East European Journal of Physics. 2. 461-469 (2026)
DOI:10.26565/2312-4334-2026-2-51 ISSN 2312-4334

STRUCTURAL, MORPHOLOGICAL AND ELECTROCHEMICAL PROPERTIES OF $NaFeO_2$ SYNTHESIZED BY SOLAR MELTING

M.S. Payzullakhanov[1,2], F.A. Giyasova[3], M.A. Yuldoshev[4]*, B.B. Gulyamov[5], F.A. Giyasov[3], A.E. Otarbaev[6], S.M. Kasimov[6], U.A. Nasritdinova[7], G.B. Rizamuxamedova[8], N.B. Xolboyeva[9], A.A. Abduvakhobov[3], A.A. Mamadaliyev[3]

[1]*Institute of Materials Science, Academy of Sciences of the Republic of Uzbekistan. Tashkent, Uzbekistan*
[2]*Fergana State Technical University, Uzbekistan*
[3]*Kimyo International University in Tashkent, Uzbekistan*
[4]*Turan International University, Namangan, Uzbekistan*
[5]*Center of Advanced Technologies, Tashkent, Uzbekistan*
[6]*Nukus State Pedagogical Institute Named After Ajiniyaz, Nukus, Uzbekistan*
[7]*Tashkent Institute of Irrigation and Agricultural Mechanization Engineers, National Research University, Uzbekistan*
[8]*Namangan State Technical University, Namangan, Uzbekistan*
[9]*Namangan State University, Namangan, Uzbekistan*
**Corresponding Author e-mail: murod.yuldoshev1993@gmail.com*
Received March 4, 2026; revised April 30, 2026; accepted May 2, 2026

This paper presents the synthesis of tetragonal sodium ferroxide ($NaFeO_2$) via a solar-furnace melting method. The resulting material is characterized by a quasi-spherical morphology, an average particle size of ~1.2 μm, high crystallinity (~ 92%), and a polydisperse distribution, which ensures efficient transport pathways and uniform electrolyte penetration. SEM analysis revealed the formation of porous aggregates of nanogranular particles (200-500 nm) with a developed specific surface area (5-10 m^2/g). DTA/TGA demonstrates multistage thermal transformations of the Na_2CO_3+Fe_2O_3 system with the formation of $NaFeO_2$ at 800-850 °C, confirming the thermal stability of the material. X-ray diffraction analysis confirmed the high crystallinity of the tetragonal phase with parameters a = 4.47 Å, c = 14.4 Å, and a coherent scattering region size of ~ 28 nm. The obtained data indicate the high structural stability and electrochemical activity of $NaFeO_2$, making it promising for use in sodium-ion batteries.
Keywords: *$NaFeO_2$; Solar furnace; Melt synthesis; Crystallinity; Microstructure; Porous aggregates; Scanning electron microscopy (SEM); X-ray diffraction (XRD); Thermal analysis (DTA/TGA); Solid-state reactions*
PACS: 68.37.Hk, 78.70.Ck, 77.84.-s

INTRODUCTION

The development of sodium-ion batteries (SIB) is one of the priority areas of modern electrochemical energy, due to the high abundance of sodium in the earth's crust, low cost of source materials and a comparatively lower environmental impact compared to lithium-ion systems [1-3]. Despite their lower theoretical energy density and less favorable ion-transport kinetics, SIBs are considered a promising alternative for stationary and large-scale energy storage systems, where safety, service life, and cost-effectiveness are key requirements [4]. The higher standard oxidation-reduction potential of the Na^+/Na pair (≈-2.71 V relative to the standard hydrogen electrode) compared to Li^+/Li leads to a decrease in the maximum cell voltage, but a rational choice of the structure and chemical composition of electrode materials can partially compensate for this disadvantage [5]. The cathode material largely determines the specific energy, operating voltage and cyclic stability of SIBs. Among the various classes of cathode compounds, $NaFeO_2$ oxide is of particular interest, combining the availability of raw materials, the environmental safety of its components, and structural compatibility with sodium ions. The theoretical specific capacity of sodium ferroxide ($NaFeO_2$) with complete extraction of Na^+ from the crystal lattice is approximately 242 $mA{\cdot}h{\cdot}g^{-1}$, which corresponds to one electron transfer per formula unit and can be estimated based on Faraday's law, taking into account the molar mass of the compound [6]. However, experimental studies [7, 8], primarily for the layered α-modification of $NaFeO_2$, demonstrate significantly lower values of reversible capacity, typically in the range of 80-120 $mA{\cdot}h{\cdot}g^{-1}$ at an average working potential of approximately 3.3 V relative to Na^+/Na. These characteristics indicate the possibility of reversible sodium intercalation and deintercalation without catastrophic structural failure at moderate charge depths, but also highlight a significant gap between the material's theoretical and practical potential. Limiting factors include low electron conductivity, limited contact area with the electrolyte, and structural transformations that occur during deep Na^+ extraction. One of the key mechanisms of $NaFeO_2$ degradation is the migration of iron ions. When charging to potentials above 3.4-3.5 V, partial release of the sodium layers occurs, accompanied by the transition of Fe cations from octahedral positions to interlayer regions. This leads to blocking of diffusion channels for Na^+, an increase in internal resistance, and a rapid loss of capacity [9, 10]. This effect significantly limits the reversible charge depth and the cathode's cyclic stability.

Cite as: M.S. Payzullakhanov, F.A. Giyasova, M.A. Yuldoshev, B.B. Gulyamov, F.A. Giyasov, A.E. Otarbaev, S.M. Kasimov, U.A. Nasritdinova, G.B. Rizamuxamedova, N.B. Xolboyeva, AA. Abduvakhobov, A.A. Mamadaliyev, East Eur. J. Phys. 2, 461 (2026), https://doi.org/10.26565/2312-4334-2026-2-51

The ionic conductivity of $NaFeO_2$ is an important parameter that determines the material's kinetic characteristics. For α-$NaFeO_2$, the activation energy for Na^+ transfer is approximately 0.31 eV in the temperature range of 306-498 K, which corresponds to the migration mechanism between octahedral sites through adjacent tetrahedral spaces, typical of layered oxides. This value indicates the possible but relatively limited transfer of sodium ions within the crystalline matrix [11].

The phase composition, morphology, and particle size are considered key factors that determine the electrochemical activity of $NaFeO_2$, according to several studies [12, 13]. In particular, for the β-modification, characterized by a tetragonal prismatic structure, specific capacity values of up to 590 $mA \cdot h \cdot g^{-1}$ were recorded after mechanical grinding and extended cycling, which is associated with increased specific surface area and improved contact between the active material and the electrolyte. These data emphasize that morphological control and optimization of Na^+ ion diffusion pathways are priority factors for improving the capacitive characteristics of cathode materials [14].

An additional effective approach to improving the electrochemical characteristics of $NaFeO_2$ is cation doping, in which the partial replacement of Fe with Mn, Ni, or Mg suppresses iron migration and stabilizes the crystal lattice, thereby increasing cyclic stability [15]. A similar effect is observed when protective coatings such as Al_2O_3 or carbon are applied, which reduce the intensity of side reactions at the electrode-electrolyte interface [16]. Electrochemical studies of the Na><$NaFeO_2$><Al system using metallic sodium Na+/Na as a reference electrode revealed a redox peak at a potential of about 0.8 V, accompanied by a specific capacity of about 110 $mA \cdot h \cdot g^{-1}$. The observed behavior is due to the sequential process of leaching and insertion of Na^+ ions followed by the Fe^{2+}/Fe^{3+} redox transition, which determines the electrochemical activity of the material [17, 18]. With increasing interest in developing cost-effective and environmentally friendly cathode materials for sodium-ion batteries, the use of compounds based on readily available elements is a relevant area of research. The tetragonal modification of $NaFeO_2$ has attracted attention due to the use of iron and the possibility of implementing reversible redox processes, but remains insufficiently studied, especially when produced by alternative high-temperature synthesis methods [19]. In this context, using a solar furnace (SF) as a source of thermal energy is a promising, energy-efficient approach.

The objective of this study is to synthesize the tetragonal modification of $NaFeO_2$ by melting in a superconducting furnace and to investigate its structural, morphological, and electrochemical properties to assess the potential of this material as a cathode for sodium-ion batteries.

This study aims to establish the temperature-dependent formation of the $NaFeO_2$ phase, determine the crystal structure and degree of crystallinity of the resulting material, analyze the morphology and particle size distribution, and investigate the electrochemical activity associated with Na^+ ion intercalation/deintercalation processes and Fe^{2+}/Fe^{3+} redox transitions.

EXPERIMENTAL SAMPLES AND MEASUREMENT METHODS

The synthesis of $NaFeO_2$ material was carried out by melting a stoichiometric mixture of $Na_2CO_3 + Fe_2O_3$ in a stream of concentrated solar radiation on a solar panel with a vertical optical axis [20, 21]. The density of the concentrated radiation flux was calculated based on the Stefan-Boltzmann equation, which describes the radiation of heated bodies:

$$Q = \varepsilon\sigma T^4 \quad (1)$$

where ε is the emissivity of the material, $\sigma=5.67\times10^{-8}$ W/m^2K^4 is the Stefan–Boltzmann constant, T is the body temperature (K).

With the emissivity of rocks being ε = 0.85, the required flux density for melting AMMP metallurgical waste (T=1750 K) was Q=50 W/cm^2. The melt was cooled by pouring it into water at a high cooling rate (~10^3°C/s). After quenching, the melt was ground to a particle size of about 60 μm and molded into cylindrical samples with a diameter of 8 mm and a height of 2 mm. The resulting cylinders were sintered at various temperatures [22-25].

X-ray diffraction (XRD) analysis of the samples was performed on a PANalytical Empyrean diffractometer with Kα radiation in Bragg-Brentano geometry (λ = 1.5418 Å) at a 2θ range of 20–60°. The slit system was selected such that the X-ray beam completely covered the sample surface over the entire 2θ range.

Surface morphology was examined using scanning electron microscopy (JEOL JSM 6510 and HITACHI FLEXSEM 100), and chemical functional groups were determined using FT-IR (SHIMADZU 8210PK). Electrical conductivity of the samples was measured by impedance using an LCR meter (frequency range 20 Hz - 500 kHz).

The relative density of the samples was calculated using the formula:

$$\rho_r = \rho_m/\rho_{dw}, \quad (2)$$

where, ρ_m is the density of the sample material, $\rho_{d.w}$= 0.98 g/cm^3 is the density of distilled water under normal conditions. For $NaFeO_2$, the relative density was ρ_r=4.07 g/cm^3.

Thermophysical properties were studied using a synchronous thermal analyzer STA PT 1600/LT (Linseis), performing simultaneously thermogravimetric analysis (TGA), differential thermal analysis (DTA), and differential scanning calorimetry (DSC). The morphology of the samples was additionally investigated using an SEM EVO MA 10 (Carl Zeiss, Germany) [26-28].

Particle size distribution was determined using a Laser Particle Size Analyzer Winner 2005. Measurements were performed using laser diffraction, which is based on recording the intensity of light scattered by particles at different

angles. The diffraction pattern was processed using Mie theory [29] to determine the volume distribution of particles in the size range from 10 nm to several millimeters.

RESULTS AND DISCUSSION

To determine the phase transformation temperatures of the studied material ($NaFeO_2$), comprehensive measurements were conducted using DTA, TGA, and calorimetry. These experiments were performed on a Na_2CO_3+Fe_2O_3 mixture in the temperature range from 27 °C to 1000 °C, and the results are presented in Fig 2.

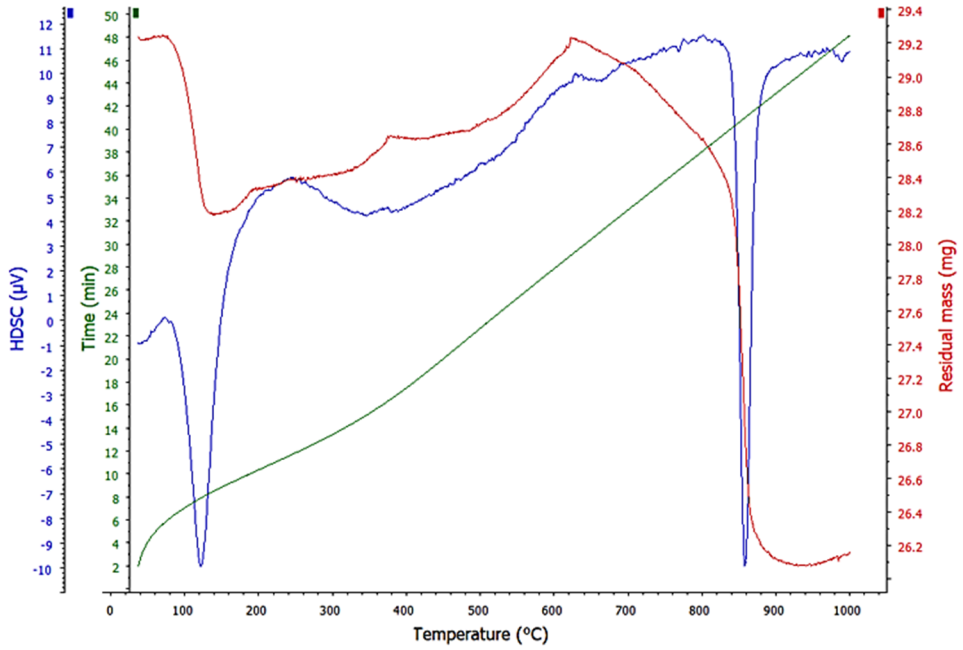

Figure 1. TG-DTA/DSC curves of a sample of the Na_2CO_3 + Fe_2O_3 mixture

In the low-temperature range of 27-150 °C, the thermogravimetric curve shows a small mass loss, while in the range of 80-120 °C, the DTA registers a distinct endothermic minimum. This thermal effect is due to the absorption of energy during the desorption of physically bound moisture, the removal of low-molecular volatile impurities from the pore space and the surface of the sample, and the dehydration of hygroscopic sodium carbonate [30, 31]:

$$Na_2CO_3 \cdot nH_2O \rightarrow Na_2CO_3 + nH_2O\uparrow \quad (3)$$

In this temperature range, the initial mass loss of the sample is $\Delta m_1 \approx 2.8\%$ of the initial mass m_0. The mass loss is expressed through the ratio:

$$\Delta m_1 = \frac{m_0 - m_{150}}{m_0} \times 100\ \% \quad (4)$$

where, m_{150} is the mass of the sample after heating to 150°C.

The DSC curve shows a pronounced endothermic effect (minimum heat flow) [32] associated with heat absorption. The enthalpy of the thermal effect was determined using the formula [33]:

$$\Delta H = \frac{1}{\beta}\int_{T_1}^{T_2} \Phi\,(T)\,dT \quad (5)$$

The enthalpy of this process, ΔH_1, was estimated from the area of the endothermic peak on the DTA curve and is $\Delta H \approx 20$-50 J/g, which corresponds to the typical range for moisture evaporation processes. The presence of the endothermic peak confirms heat absorption during desorption and removal of volatile components.

In the medium temperature range (150-500 °C), a more gradual change in sample mass occurs – 3.5 %, and the total mass loss by 500 °C is 6.3%. The TG curve indicates a gradual decrease in mass, which may be associated with the thermal decomposition of organic components, dehydroxylation, or the removal of chemically bound water. In the range of 200–500 °C, smoothed deviations in heat flow are observed, corresponding to overlapping endo- and exothermic processes [34, 35]. The enthalpies of these effects are estimated as moderate, not exceeding 100 J/g.

With a further increase in temperature in the range of 500-800 °C, the DTA curve shows an increase in thermal effects, which is associated with the rearrangement of the material structure, phase transformations, and the onset of crystallization. The change in mass in this range does not exceed 1.7 %, remains moderate, and indicates the relative thermal stability of the main inorganic matrix of the sample. The observed exothermic effect is due to the onset of solid-phase interaction between Na_2CO_3 and DTA with the formation of sodium-iron oxide phases, in particular $NaFeO_2$ [36]:

$$Na_2CO_3 + Fe_2O_3 \rightarrow 2NaFeO_2 + CO_2\uparrow \quad (6)$$

The exothermic effect indicates the release of heat during the formation of a new crystalline structure; the magnitude of the thermal effect is 50-100 J/g.

In the region of intense transformations, at temperatures of 800-850 °C, a sharp exothermic peak is recorded on the DTA curve, accompanied by a sudden decrease in residual mass of approximately 4.6 %. This effect is associated with the intense decomposition of Na_2CO_3 and the active reaction with Fe_2O_3, releasing carbon dioxide:

$$Na_2CO_3 \rightarrow Na_2O + CO_2\uparrow \quad (7)$$

A large peak area indicates the occurrence of an intense phase or structural transformation, and a semi-quantitative estimate of the process enthalpy is 100–300 J/g, corresponding to high-energy phase and chemical transformations [37].

Upon further heating to 1000 °C, the sample mass stabilizes, and the thermal effects become less pronounced. Reaching a residual mass of 88-90 % of the initial mass is associated with the completion of decarbonization processes and the formation of thermodynamically stable sodium-iron oxide phases. DTA and TGA data for the initial Na_2CO_3+Fe_2O_3 mixture revealed the removal of adsorbed moisture and volatile components in the range of 27-330 °C, as well as a pronounced exothermic effect at 850 °C, corresponding to the completion of the $NaFeO_2$ phase formation [38].

Next, to determine the phase state and structure of the material, X-ray phase analysis was performed (Fig. 2).

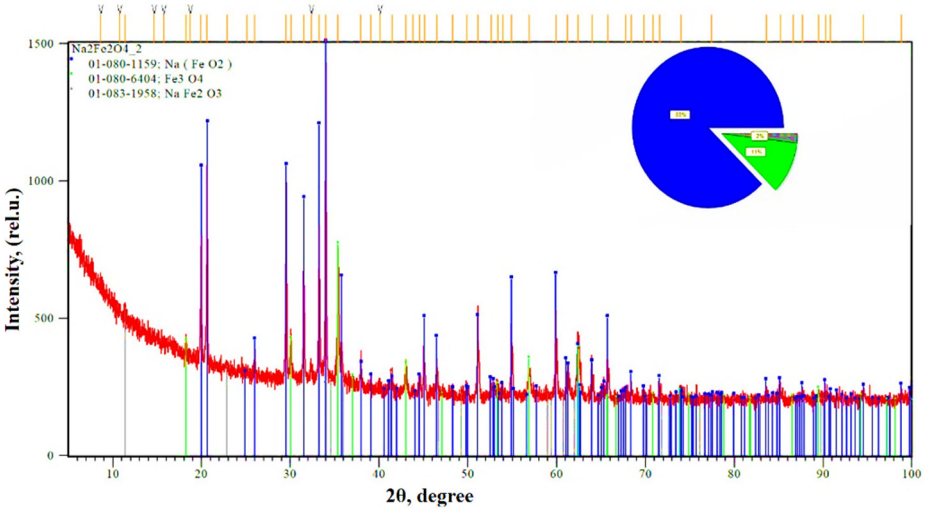

Figure 2. XRD pattern of $NaFeO_2$ synthesized by the melting method in SP

Figure 3 shows the X-ray diffraction pattern of a $NaFeO_2$ sample obtained from a melt in a solar synthesis facility. X-ray phase analysis of the pattern indicates the formation of a highly crystalline material, as evidenced by the presence of intense and narrow diffraction reflections. The set of main diffraction maxima is correctly indexed within the tetragonal crystal structure of $NaFeO_2$, indicating the successful formation of the target phase under high-temperature solar synthesis conditions. Based on the experimental positions of the diffraction peaks, the interplanar distances were calculated and the reflections were indexed. The interplanar distances d were determined using Bragg's law [39]:

$$n\lambda = 2d\sin\theta, \quad (8)$$

where, λ is the X-ray wavelength, θ is the diffraction angle, and n=1 is the reflection order. For the tetragonal crystal system, the lattice parameters were calculated using the corresponding relationships between interplanar spacings and Miller indices. The calculation results are presented in Table 1.

Table 1. X-ray structural parameters of $NaFeO_2$ synthesized from the melt

Peak no.	2θ, degree	Interplanar distance (d), Å	Miller indices (hkl)	Half-width at half maximum (β), degree	Relative intensity, %
1	18.5	4.79	(003)	0.28	100.0
2	32.0	2.80	(104)	0.30	96,7
3	37.2	2.41	(110)	0.32	80.0
4	43.4	2.08	(113)	0.34	53.3
5	57.4	1.60	(116)	0.36	33.3

The most intense diffraction maxima were recorded at angles of 2θ ≈ 18.5° and 32.0°, which corresponded to the (003) and (104) crystallographic planes. The interplanar distances calculated using Bragg's law were approximately 4.79 Å and 2.80 Å, respectively. Using the (003) reflection, we determined the lattice parameter c=14.4 Å, while a joint analysis of the (003) and (104) reflections yielded a parameter value of a=4.47 Å [40, 41]. Comparison of the obtained unit cell parameters

with the literature data [42] for tetragonal $NaFeO_2$ confirms the preservation of structural order during synthesis from the melt. The unit cell volume is V=144 Å³, and the degree of crystallinity of the material reaches 92 %. The half-width at half maximum (β) of the peak for the most intense reflection (104) is about 0.30°, indicating a high degree of crystallinity of the material and a relatively low level of microdeformations of the crystal lattice. Based on the β values, the average size of the coherent scattering regions, estimated using the Scherrer formula [43]:

$$D=K\lambda/\beta\cos\theta, \quad (9)$$

where K is the shape factor (0.9) and is 28 nm, which is typical for materials obtained under conditions of rapid cooling of the melt.

Analysis of the diffraction peaks indicates minor distortions in the $NaFeO_2$ crystal lattice relative to the ideal tetragonal structure. The absence of pronounced splitting of the diffraction maxima and the small β value reflect a weak monoclinic distortion of the structure. Low-intensity additional reflections were detected in the diffraction pattern, presumably corresponding to iron oxides Fe_2O_3 and Fe_3O_4, the appearance of which is likely associated with partial non-stoichiometry and local oxidation of iron under high-temperature solar synthesis conditions [44, 45]. However, the low intensity of these reflections relative to the main peaks of $NaFeO_2$ allows us to consider the material obtained as predominantly single-phase.

Based on these data, a generalized analysis of thermal transformations in the Na_2CO_3+Fe_2O_3 system was also carried out using DTA/TGA methods in the temperature range from room temperature to above 850 °C (Table 2).

Table 2. Characterization of thermal transformations in the Na_2CO_3+Fe_2O_3 system based on DTA/TGA and XRD data

Temperature range, °C	Δm, %	Thermal effect (DTA/DSC)	Enthalpy of the process, ΔH, J/g	The main process	Phase state (XRD)
27-150	2.8	Endothermic	20-50	Desorption of adsorbed water, removal of volatile components	Na_2CO_3+Fe_2O_3
150-500	3.5	Weak endo/exothermic	≤ 100	Dehydroxylation, removal of chemically bound water, surface activation	Na_2CO_3+Fe_2O_3
500-800	1.7	Exothermic	50-100	The beginning of the solid-phase reaction, structural rearrangement, the formation of $NaFeO_2$	Na_2CO_3+Fe_2O_3+$NaFeO_2$
800-850	4.6	Intense exothermic	100-300	Decarbonization, active formation of $NaFeO_2$, phase transition	$NaFeO_2$+Fe_2O_3
> 850	≈ 0	Absent	-	Formation of a thermodynamically stable phase of $NaFeO_2$	$NaFeO_2$ (main)

The table presents mass loss values, the nature of thermal effects, the predominant processes, and the phase composition determined by XRD. The results obtained allow for a comprehensive characterization of the thermal stability of the system's components and the sequence of phase transformations upon heating.

The microstructural features of $NaFeO_2$, studied by scanning electron microscopy, are shown in Figure 4 at a magnification of ×1000.

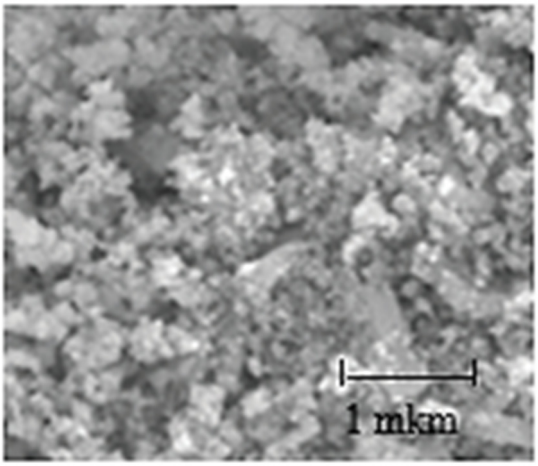

Figure 4. SEM micrograph of the surface of a sample of $NaFeO_2$ material

The image scale corresponds to 1 μm, enabling detailed assessment of the particles' morphological features. As can be seen in Fig 4, the particles have a quasi-spherical shape and exhibit a high degree of agglomeration, with their sizes varying from 0.5 to 10 μm, with a maximum particle number of approximately 1.2 μm. The surface microstructure is characterized by a coarse-grained and porous texture with the formation of aggregates of small crystalline grains approximately 200-500 nm in size, indicating material growth through crystallization from the melt with subsequent aggregation of crystals

into larger aggregates. The high degree of surface roughness provides a specific surface area of approximately 5-10 m^2/g, which increases the contact area with the electrolyte and facilitates the diffusion of Na^+. Moreover, the particle distribution is relatively uniform, without pronounced defects or cracks, reflecting the high crystalline integrity of the material [46-48].

To evaluate the particle size and distribution of the synthesized $NaFeO_2$, laser transmission spectroscopy (LPSA/LD) was used, as shown in Fig 5.

The obtained data showed an asymmetric particle volume distribution with a distinct main peak at approximately 1.5 μm. Analysis of the particle volume fraction revealed that approximately 70 % of the powder consisted of particles up to 5 μm in diameter, indicating the predominance of the finely dispersed component. The median particle size (d_{50}) was 1.5 μm, which corresponded to the position of the main distribution peak. The particle spread from d_{10}=0.5 μm to d_{90}=7 μm corresponds to a wide polydisperse spectrum (PDI ≈ 4.3). This distribution is characterized by the presence of both small and relatively large particles [49, 50]. Finely dispersed particles provide a significant reactive surface, which can contribute to higher reaction rates in thermal and electrochemical processes. Large particles, including agglomerates up to 20 μm in size, are relatively rare, which minimizes potential problems with material homogeneity and deterioration of properties during pressing or forming electrodes [51, 52].

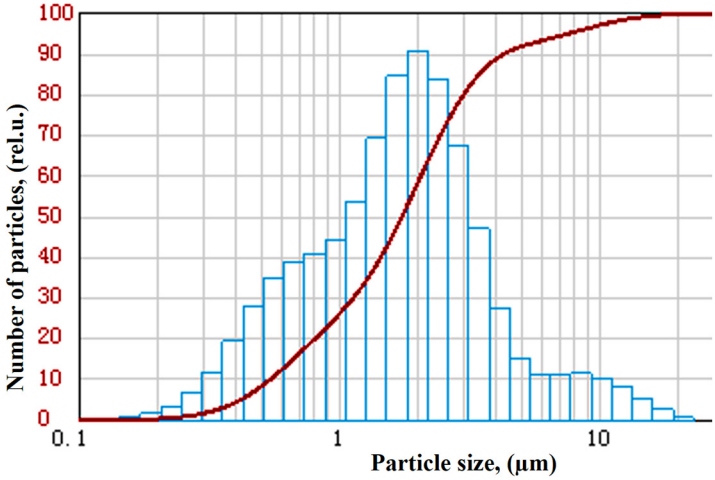

Figure 5. Particle distribution spectrum of $NaFeO_2$ by LPSA/LD method

CONCLUSIONS

Sodium ferroxide ($NaFeO_2$) was synthesized via solar melting, yielding quasi-spherical particles with an average size of 1.2 μm and a crystallinity of 92%. These characteristics facilitate uniform electrolyte penetration and the formation of efficient Na^+ transport pathways. The synthesis method significantly influences the structural and morphological properties of $NaFeO_2$. High-temperature processes, including melt synthesis, enable the formation of a material with a high degree of crystallinity and minimal secondary-phase content.

The resulting $NaFeO_2$ powder exhibits a polydisperse particle distribution, with a predominance of small and medium-sized particles, thereby ensuring a combination of high reactivity and structural stability. The variety of particle sizes also affects powder packing and the density of pressed samples, both of which are important to consider when developing electrochemical cells. SEM data confirm that the synthesized $NaFeO_2$ forms a microstructure with porous aggregates of nanogranular particles (200-500 nm) and a developed specific surface area (5-10 m^2/g), which positively impacts its functional properties.

Thermal studies of the Na_2CO_3+Fe_2O_3 system have shown that the formation of tetragonal $NaFeO_2$ occurs at high temperatures (500-850°C) through successive stages of moisture desorption, dehydration, and solid-phase reactions. Low-temperature effects (ΔH≈20-50 J/g) are due to the removal of adsorbed and chemically bound water, medium-temperature effects (ΔH≈50-100 J/g) are due to gradual structural rearrangement and dehydroxylation, and at 800-850 °C intense exothermic processes are observed with the decomposition of Na_2CO_3 and the formation of $NaFeO_2$ (ΔH≈100-300 J/g). DTA/TGA analysis revealed that thermal transformations occur in several stages, with a total mass loss of approximately 10-12 %, primarily due to dehydration and CO_2 evolution. The highest activity of solid-phase interactions and the formation of the target phase are observed at 800-850°C, confirming the material's thermal stability and enabling us to determine the optimal synthesis conditions for its functional application.

X-ray diffraction (XRD) analysis revealed that $NaFeO_2$ synthesized by solar melting forms a highly crystalline tetragonal material with unit cell parameters a=4.47 Å, c=14.4 Å, and a volume V=144 $Å^3$. The presence of the main diffraction peaks (003) and (104), their width (0.30°), and the calculated size of the coherent scattering regions (28 nm) confirm the high crystallinity of the material and low microstrain. Trace additional reflections of Fe_2O_3 and Fe_3O_4 do not disrupt the single-phase nature of the sample.

These comprehensive data confirm that solar melting enables the synthesis of stable tetragonal $NaFeO_2$ with high electrochemical activity and cycling stability, creating favorable conditions for its application in sodium-ion batteries.

ORCID

F.A. Giyasova, https://orcid.org/0000-0003-0746-4986; **M.A. Yuldoshev,** https://orcid.org/0000-0002-9722-9439
B.B. Gulyamov, https://orcid.org/0009-0008-8838-4278; **F.A. Giyasov,** https://orcid.org/0009-0003-9882-0655
S.M. Kasimov, https://orcid.org/0009-0009-5445-372X; **A.E. Otarbaev,** https://orcid.org/0009-0009-7942-9398
N.B. Xolboyeva, https://orcid.org/0009-0007-7480-5572

REFERENCES

[1] A.F. Salam, X. Zheng, Z. Chen, Y. Liao, D.K. Kim, S.S. Mofarah, P. Koshy, *et al*., "Sodium-ion battery development since 2020 with future perspectives," Journal of Materials Chemistry A, **14**, 9115-9137 (2026). https://doi.org/10.1039/D5TA07726E
[2] Y. Li, "Review of sodium-ion battery research," Advances in Engineering Innovation, **16**(3), 31-37 (2025). https://doi.org/10.54254/2977-3903/2025.21919
[3] S.F. Samadov, N.V.M. Trung, A.A. Sidorin, S.I. Ibragimova, S.H. Jabarov, M.A. Yuldoshev, O.S. Orlov, Y.I. Aliyev, Micro and Nanostructures, **209**, 208451 (2026). https://doi.org/10.1016/j.micrna.2025.208451
[4] P. Phogat, S. Dey, and M. Wan, "Comprehensive review of Sodium-Ion Batteries: Principles, Materials, Performance, Challenges, and future Perspectives," Materials Science and Engineering: B, **312**, 117870 (2025). https://doi.org/10.1016/j.mseb.2024.117870
[5] L. Zhao, T. Zhang, W. Li, T. Li, L. Zhang, X. Zhang, and Zh. Wang, "Engineering of Sodium-ion Batteries: Opportunities and Challenges," Engineering, **24**(5), (2023). https://doi.org/10.1016/j.eng.2021.08.032
[6] J.Y. Hwang, S.T. Myung and Y.K. Sun, "Sodium-ion batteries: present and future," Chem. Soc. Rev. **46**, 3529-3614 (2017). https://doi.org/10.1039/C6CS00776G
[7] J.-Y. Hwang, S.-T. Myung, and Y.-K. Sun, "Sodium-ion batteries: present and future," Chem. Soc. Rev. **46**, 3529-3614 (2017). https://doi.org/10.1039/C6CS00776G
[8] J. Jayachitra, J.R. Joshua, A. Balamurugan, N. Sivakumar, V. Sharmila, S. Shanavas, M.A. Haija, *et al*., "High electrode performance of hydrothermally developed activated C coated O_3-$NaFeO_2$ electrode for Na-ion batteries applications," Ceramics International, **49**(1), 48-56 (2023). https://doi.org/10.1016/j.ceramint.2022.07.110
[9] Y. Li, Y. Gao, X. Wang, Xi Shen, Q. Kong, R. Yu, G. Lu, *et al*., "Iron migration and oxygen oxidation during sodium extraction from $NaFeO_2$," Nano Energy, **47**, 519-526 (2018). https://doi.org/10.1016/j.nanoen.2018.03.007
[10] Zh.Ch. Jian, J.X. Guo, Y. Liu, Y. Zhu, J. Wang, and Y. Xiao, "Cation migration in layered oxide cathodes for sodium-ion batteries: fundamental failure mechanisms and practical modulation strategies," Chem. Sci, **15**, 19698-19728 (2024). https://doi.org/10.1039/D4SC05206D
[11] M.C. Blesa, E. Moran, C. León, J. Santamaria, J.D. Tornero, and N. Menéndez, "α-$NaFeO_2$: ionic conductivity and sodium extraction," Solid State Ionics, **126**(1-2), 81-87 (1999). https://doi.org/10.1016/S0167-2738(99)00145-9
[12] R.D. McAuliffe, G.E. Kamm, M.J. McDermott, R.P. Hermann, N.V. Garcia, R.L. Sacci, K.A. Persson, *et al*., "Direct Mechanochemical Synthesis, Phase Stability, and Electrochemical Performance of α $NaFeO_2$," Inorganic Chemistry, **62**(8), 3358-3367 (2023). https://doi.org/10.1021/acs.inorgchem.2c03286
[13] M.A. Rusho, T.A. Ahmed, L.H. Saleh, S.W. Ghori, E. Muniyandy, S. Usanov, M. Latipova, *et al*., "Design and synthesis of decorated palladium nanoparticles on chitosan-tannic acid modified magnetic nanoparticles and evaluation of its catalytic application in the Heck coupling reactions," Journal of Organometallic Chemistry, **1039**, 123773 (2025). https://doi.org/10.1016/j.jorganchem.2025.123773
[14] H. Watanabe, H. Usui, Y. Domi, T. Nishida, K. Uetake, T. Tanaka, H. Kurokawa, *et al*., "$NaFeO_2$: Possible Materials for Anode and Cathode of Na-Ion Batteries," ACS Electrochemistry, **1**(1), 73-81 (2025). https://doi.org/10.1021/acselectrochem.4c00024
[15] V. Shipitsyn, *et al*., "Advancing Sodium-Ion Battery Cathodes: A Low-Cost, Eco-Friendly Mechanofusion Route from TiO_2 Coating to Ti^{4+} Doping," Chem. Mater. **37**, 6059-6068 (2025). https://doi.org/10.1021/acs.chemmater.5c01485
[16] X. Zhao, Qi Liu, W. He, D. Mu, L. Li, R. Chen, and F. Wu, "Uniform Al_2O_3 coating for improved cycling stability of O_3-type sodium-ion batteries cathode: Mechanisms and performance insights," Journal of Energy Storage, **131**, Part A, 117548 (2025). https://doi.org/10.1016/j.est.2025.117548
[17] J. Zhao, L. Zhao, N. Dimov, Sh. Okada, and T. Nishida, "Electrochemical and thermal properties of α-$NaFeO_2$ cathode for Na-ion batteries," Journal of the Electrochemical Society, **160**(5), A3077-A3081 (2013). https://doi.org/10.1149/2.007305jes
[18] N. Yabuuchi, K. Kubota, M. Dahbi, and Sh. Komaba, "Research Development on Sodium-Ion Batteries," Chem. Rev. **114**(23), 11636-11682 (2014). https://doi.org/10.1021/cr500192f
[19] M.G.D. Guaita, O.J. Oliveira, P.R. Silva, L.H. Antonia, and A. Urbano, "New $NaFeO_2$ synthesis route for green sodium-ion batteries," Green Materials, **11**(3), 115-124 (2022). https://doi.org/10.1680/jgrma.21.00050
[20] M.S. Paizullakhanov, F.A. Giyasova, Kh.N. Bakhronov, M.A. Yuldoshev, A.A. Mamadaliev, F.A. Giyasov, F.T. Akbarova, *et al*., "Investigation of the Processes Involved in the Formation of Pyroxene Materials during Solar Melting in a Large Solar Furnace," Journal of Ovonic Research, **22**(1), (2026). https://doi.org/10.15251/JOR.2026.221.51
[21] M.S. Payzullakhanov, F.A. Giyasova, M.A. Yuldoshev, Ch.X. Toshpulatov, R.U. Ernazarov, F.A. Giyasov, A. Urishev, *et al*., East Eur. J. Phys. (1), 233 (2026). https://doi.org/10.26565/2312-4334-2026-1-25
[22] M.S. Paizullakhanov, O.R. Parpiev, F.N. Ernazarov, *et al*., "Features of Barium–Strontium Cobaltite as a Catalyst for Hydrogen Generation," Glass Phys. Chem. **50**, 55–60 (2024). https://doi.org/10.1134/S1087659623601181
[23] M.S. Paizullakhanov, N.K. Karshieva, F.N. Ernazarov, *et al*., "Studying the Possibility of Applying Barium-Strontium Cobaltite in Hydrogen Energy," Therm. Eng. **71**, 280–284 (2024). https://doi.org/10.1134/S0040601524030054
[24] N.Yu. Sharibaev, A.Q. Ergashov, S.B. Fazliddinov, R.G. Ikramov, M.A. Yuldoshev, and A.A. Abdulxayev, "Photoelectric characteristics of TiO2-based on thin-film solar elements with ruthenium (II) compounds," Journal of Ovonic Research, **21**(6), (2025). https://doi.org/10.15251/JOR.2025.216.859
[25] Sh. I. Klychev, S. A. Bakhramov, O. R. Parpiev, M. S. Paizullakhanov, L. S. Suvonova, D. E. Kadyrgulov, E. K. Matjanov, *et al*., "Optical-Energy Characteristics and Heating Temperatures in Small Single-Mirror Solar Furnaces," Applied Solar Energy, **60**(5), 703-707 (2025). https://doi.org/10.3103/S0003701X24602394

[26] Sh.B. Utamuradova, F.A. Giyasova, K.N. Bakhronov, M.A. Yuldoshev, M.R. Bekchanova, and B. Ismatov, "Current Transfer Mechanism in A Thin-Based Heterosystem Based on A^2B^6 Compounds," East Eur. J. Phys. (3), 325 (2025). https://doi.org/10.26565/2312-4334-2025-3-31
[27] M.A. Yuldoshev, Z.T. Azamatov, A.B. Bakhromov, and M.R. Bekchanova, East Eur. J. Phys. (4), 250 (2024), https://doi.org/10.26565/2312-4334-2024-4-25
[28] F.A. Giyasova, A.Z. Rakhmatov, Kh.N. Bakhronov, M.A. Yuldoshev, F.A. Giyasov, A.N. Olimov, and N.A. Sattarov, East Eur. J. Phys. (4), 397 (2025). https://doi.org/10.26565/2312-4334-2025-4-38
[29] A. Mudroch, J.M. Azcue, and P. Mudroch, *Manual of Physico-Chemical Analysis of Aquatic Sediments*, (CRC Press, 1996).
[30] N. Đorđević, S. Mihajlović, G. Jovanović, and B. Marković, "DTA/TG analysis of mechanochemically activated sodium carbonate," Podzemni Radovi, (38), 47-55 (2021). https://doi.org/10.5937/podrad2138047Q
[31] J. Matrasulov, J.R. Yusupov, and A.A. Saidov, "Fast forward evolution in heat equation: Tunable heat transport in adiabatic regime," Phys. Chem. Math, **14**(4), 421-427 (2023). https://doi.org/10.17586/2220-8054-2023-14-4-421-427
[32] A.J. Müller, and R.M. Michell, "Differential Scanning Calorimetry of Polymers" in: *Polymer Morphology*, (2016), pp.72-99, https://doi.org/10.1002/9781118892756
[33] P. Kaur, M. Singh, and P. Birwal, "Differential Scanning Calorimetry (DSC) for the Measurement of Food Thermal Characteristics and Its Relation to Composition and Structure," in: *Techniques to Measure Food Safety and Quality*, edited by M.S. Khan, and M.Sh. Rahman, (Springer, 2021). https://doi.org/10.1007/978-3-030-68636-9_13
[34] M. Labus, M. Irena, and K. Ziemianin, "Thermal Decomposition Processes in Relation to the Type of Organic Matter, Mineral and Maceral Composition of Menilite Shales," Energies, **16**(11), 4500 (2023). https://doi.org/10.3390/en16114500
[35] F.A. Giyasova, Kh.N. Bakhronov, M.A. Yuldoshev, I.B. Sapaev, R.G. Ikramov, F.A. Giyasov, M.R. Bekchanova, *et al*., "Study of The Influence of Temperature on the Transitions of the CdS/Si/CdTe Heterosystem," East Eur. J. Phys. (4), 461 (2025). https://doi.org/10.26565/2312-4334-2025-4-47
[36] G.P. Luo, Q. Sun, Y.B. Wang, and J.G. Zhu, "Influence of Na_2O Content on Lattice Structures of Iron Oxides during Reduction Process of Fe_2O_3 Briquetting," in: *4th Annual International Conference on Material Science and Engineering, (ICMSE 2016)*, pp. 0118-0126.
[37] H. Takasu, H. Hoshino, Y. Tamura, S.T. Kim, and Y. Kato, "Sodium Ferrite/Carbon Dioxide Reactivity for High Temperature Thermochemical Energy Storage," ISIJ International, **59**(4), 715-720 (2019). https://doi.org/10.2355/isijinternational.ISIJINT-2018-182
[38] J. Huang, T. Furukawa, and K. Aoto, "High temperature behavior of Na-Fe oxides in H_2O+CO_2 atmosphere," Journal of Physics and Chemistry of Solids, **66**(2-4), 388-391 (2005). https://doi.org/10.1016/j.jpcs.2004.06.084
[39] T. Arlt, R.J. Angel, R. Miletich, Th. Armbruster, and T. Peters, "High-pressure P21/c-C2/c phase transitions in clinopyroxenes; influence of cation size and electronic structure," American Mineralogist, **83**, 1176-1181 (1998). https://doi.org/10.2138/am-1998-11-1205
[40] N. Kuganathan, N. Kelaidis, and A. Chroneos, "Defect Chemistry, Sodium Diffusion and Doping Behaviour in $NaFeO_2$ Polymorphs as Cathode Materials for Na-Ion Batteries: A Computational Study," Materials, **12**(19), 3243 (2019). https://doi.org/10.3390/ma12193243
[41] G.M. Milibaeva, H.T. Yusupov, D.G. Berdiyorova, Y. Rakhimova, M. Yusupov, A. Chaves, and Kh. Rakhimov, "Wave packet propagation through square and triangular patterned circular potential scatterers in graphene," Physica Scripta, **100**(12), 125945 (2025). https://doi.org/10.1088/1402-4896/ae2a7d
[42] N. Yabuuchi, H. Yoshida, and S. Komaba, "Crystal structures and electrode performance of alpha-$NaFeO_2$ for rechargeable sodium batteries," Electrochemistry, **80**(10), 716-719 (2012). https://doi.org/10.5796/electrochemistry.80.716
[43] D. Balzar, "X-Ray Diffraction Line Broadening: Modeling and Applications to High-Tc Superconductors," J. Res. Natl. Inst. Stand. Technol. **98**(3), 321-353 (1993). https://doi.org/10.6028/jres.098.026
[44] O. Ergashev, Kh. Bakhronov, F. Giyasova, E. Nazirakhon, R. Yunusova, V. Gaffarova, O. Ochilova, *et al*., "Energy Characteristics, Adsorption Kinetics, and Mechanism of Triethylamine Adsorption on CsZSM-5 Zeolite," J. Appl. Organomet. Chem, **6**(1), 43-52 (2026). https://doi.org/10.48309/JAOC.2026.546865.1334
[45] B. Silván, E. Gonzalo, L. Djuandhi, F. Fauth, N. Sharma, and D. Saurel, "On the dynamics of transition metal migration and its impact on the performance of layered oxides for sodium-ion batteries: $NaFeO_2$ as a case study," Journal of Materials Chemistry A, **6**(31) (2018). https://doi.org/10.1039/C8TA02473A
[46] Y. Zhao, Q. Lai, Y. Hao, H. Zeng, H. Chu, and Zh. Lin, "A porous spherical aggregation of $Li_4Mn_5O_{12}$ nanorods and its electrochemical performance," Journal of Power Sources, **195**(13), 4400-4405 (2010). https://doi.org/10.1016/j.jpowsour.2010.01.072
[47] M. Müller, L. Schneider, N. Bohn, J.R. Binder, and W. Baue, "Effect of Nanostructured and Open-Porous Particle Morphology on Electrode Processing and Electrochemical Performance of Li-Ion Batteries," ACS Appl. Energy Mater, **4**, 1993-2003 (2021). https://doi.org/10.1021/acsaem.0c03187
[48] Sh.I. Nabiyev, Kh.N. Bozorov, *et al*., "Study of the Formation of Radiation Defects in Irradiated Silicon Samples, Doped with Chromium Atoms," East Eur. J. Phys. (1), 228 (2026). https://doi.org/10.26565/2312-4334-2026-1-24
[49] Zh. Sun, N. Ya, R.C. Adams, and F.S. Fang, "Particle size specifications for solid oral dosage forms: A regulatory perspective," American Pharmaceutical Review, **13**(4), 68-73 (2010).
[50] A.J.R. Rennie, V.L. Martins, R.M. Smith, and P.J. Hall, "Influence of Particle Size Distribution on the Performance of Ionic Liquid-based Electrochemical Double Layer Capacitors," Scientific Reports, **6**(1), 22062 (2016). https://doi.org/10.1038/srep22062
[51] H. Liu, X. Cheng, Y. Chong, Hong Yuan, and J. Huang, "Advanced electrode processing of lithium-ion batteries: A review of powder technology in battery fabrication," Particuology, **57**, 56-71 (2021). https://doi.org/10.1016/j.partic.2020.12.003

[52] M.S. Payzullakhanov, Sh.D. Payziyev, and S.Kh. Suleymanov, "Modeling of Processes of Heating and Cooling of Materials in a Solar Furnace," Applied Solar Energy, **55**(6), 404-408 (2019). https://doi.org/10.3103/S0003701X19060082

СТРУКТУРНІ, МОРФОЛОГІЧНІ ТА ЕЛЕКТРОХІМІЧНІ ВЛАСТИВОСТІ $NaFeO_2$, СИНТЕЗОВАНОГО СОНЯЧНИМ ПЛАВЛЕННЯМ

М.С. Пайзуллаханов[1,2], Ф.А. Гіясова[3], М.А. Юлдошев[4], Б.Б. Гулямов[5], Ф.А. Гіясов[3], А.Е. Отарбаєв[6], С.М. Касімов[6], U.A. Насрітдінова[7], Г.Б. Різамухамедова[8], Н.Б. Холбоєва[9], А.А. Абдувахобов[3], А.А. Мамадалієв[3]

[1]Інститут матеріалознавства Академії наук Республіки Узбекистан. Ташкент, Узбекистан

[2]Ферганський державний технічний університет, Узбекистан

[3]Міжнародний університет Кімьо в Ташкенті, Узбекистан

[4]Міжнародний університет Туран, Наманган, Узбекистан

[5]Центр передових технологій, Ташкент, Узбекистан

[6]Нукусський державний педагогічний інститут імені Аджиніяза, Нукус, Узбекистан

[7]Ташкентський інститут інженерів іригації та механізації сільського господарства, Національний дослідницький університет, Узбекистан

[8]Наманганський державний технічний університет, Наманган, Узбекистан

[9]Наманганський державний університет, Наманган, Узбекистан

У цій статті представлено синтез тетрагонального фероксиду натрію ($NaFeO_2$) методом плавлення в сонячній печі. Отриманий матеріал характеризується квазісферичною морфологією, середнім розміром частинок ~1,2 мкм, високою кристалічністю (~ 92%) та полідисперсним розподілом, що забезпечує ефективні шляхи транспорту та рівномірне проникнення електроліту. SEM-аналіз виявив утворення пористих агрегатів наногранулярних частинок (200-500 нм) з розвиненою питомою поверхнею (5-10 м²/г). DTA/TGA демонструє багатоступеневі термічні перетворення системи Na_2CO_3+Fe_2O_3 з утворенням $NaFeO_2$ при 800–850 °C, що підтверджує термічну стабільність матеріалу. Рентгеноструктурний аналіз підтвердив високу кристалічність тетрагональної фази з параметрами a = 4,47 Å, c = 14,4 Å та розміром області когерентного розсіювання ~ 28 нм. Отримані дані свідчать про високу структурну стабільність та електрохімічну активність $NaFeO_2$, що робить його перспективним для використання в натрій-іонних акумуляторах.

Ключові слова: *$NaFeO_2$; сонячна піч; синтез розплаву; кристалічність; мікроструктура; пористі агрегати; скануюча електронна мікроскопія (SEM); рентгенівська дифракція (XRD); термічний аналіз (DTA/TGA); твердофазні реакції*